Nanometer resolution imaging and tracking of fluorescent molecules with minimal photon fluxes

Francisco Balzarotti,[1,2,3]*† **Yvan Eilers,**[1,2,3]* **Klaus C. Gwosch,**[1,2,3]* **Arvid H. Gynnå,**[4] **Volker Westphal,**[1,2,3]
Fernando D. Stefani,[5,6] **Johan Elf,**[4] **Stefan W. Hell**[1,2,3]†

[1]Department of NanoBiophotonics, Max Planck Institute for Biophysical Chemistry, Göttingen, Germany. [2]Department of Optical Nanoscopy, Max Planck Institute for Medical Research, Heidelberg, Germany. [3]Optical Nanoscopy Division, German Cancer Research Center (DKFZ), Heidelberg, Germany. [4]Department of Cell and Molecular Biology, Science for Life Laboratory, Uppsala University, Uppsala, Sweden. [5]Centro de Investigaciones en Bionanociencias (CIBION), Consejo Nacional de Investigaciones Científicas y Técnicas (CONICET), Buenos Aires, Argentina. [6]Departamento de Física, Facultad de Ciencias Exactas y Naturales, University of Buenos Aires, Buenos Aires, Argentina.

*These authors contributed equally to this work.

†Corresponding author. E-mail: stefan.hell@mpibpc.mpg.de (S.W.H.); francisco.balzarotti@mpibpc.mpg.de (F.B.)

We introduce MINFLUX, a concept for localizing photon emitters in space. By probing the emitter with a local intensity minimum of excitation light, MINFLUX minimizes the fluorescence photons needed for high localization precision. A 22-fold reduction of photon detections over that required in popular centroid-localization is demonstrated. In superresolution microscopy, MINFLUX attained ~1-nm precision, resolving molecules only 6 nm apart. Tracking single fluorescent proteins by MINFLUX increased the temporal resolution and the number of localizations per trace by 100-fold, as demonstrated with diffusing 30S ribosomal subunits in living *Escherichia coli*. As conceptual limits have not been reached, we expect this localization modality to break new ground for observing the dynamics, distribution, and structure of macromolecules in living cells and beyond.

Superresolution fluorescence microscopy or nanoscopy methods, such as those called STED (*1*, *2*) and PALM/STORM (*3–5*), are strongly impacting modern biology because they can discern fluorescent molecules or features that are closer together than half the wavelength of light. Despite their different acronyms, all these methods ultimately distinguish densely packed features or molecules in the same way: only one of them is allowed to fluoresce, while its neighbors have to remain silent (*6*). Although this sequential on- and off- switching of molecular fluorescence is highly effective at making neighboring molecules discernible, it does not provide their location in space, which is the second requirement for obtaining a superresolution image. In this regard, these methods strongly depart from each other, broadly falling into two categories.

In the so-called coordinate-targeted versions (*6*), which most prominently include STED microscopy, the position of the emitting molecules is established by illuminating the sample with a pattern of light featuring points of ideally zero intensity, such as a doughnut-shaped spot or a standing wave. The intensity and the wavelength of the pattern are adjusted such that molecular fluorescence is switched off (or on) everywhere—except at the minima where this process cannot happen. As it is 'injected' by the incoming pattern, the emitter position is always known through the device controlling the position of the minima. In contrast, the coordinate-stochastic superresolution modalities PALM/STORM switch on (and off) the molecules individually and randomly in space, implying that the molecular position is established subsequently, using emitted rather than injected photons. The emitter position is estimated from the centroid of the fluorescence diffraction pattern produced by the emitter on a camera (*7*). Called 'localization', this process can reach a precision given by the standard deviation of the diffraction fluorescence pattern ($\sigma_{PSF} \approx 100$ nm) divided by $\sqrt{N}$, with N being the number of detected photons (*8–11*). While $N = 400$ should yield precisions of $\sigma \approx 5$ nm, obtaining these limits is commonly challenged by other factors such as the typically unknown orientation of the fluorophore emission dipole (*12*, *13*).

Camera based localization is also the method of choice for tracking individual molecules (*14–16*). Here, the sum of molecular emissions determines the track length, whereas the emission rate determines the spatio-temporal resolution. Unfortunately, large emission rates reduce the track length by exacerbating bleaching. Alternatively, the molecule can be localized with scanning confocal arrangements (*17*), but this also needs large photon numbers N. Therefore, improving localization has so far concentrated on increasing molecular emission, particularly through anti-bleaching agents (*18*), special fluorophores (*19*), cryogenic conditions (*20*),

transient (fluorogenic) labels (*21, 22*), and fluorophore-metal interactions (*23*). However, apart from the fact that all these remedies entail restrictions when applied to (living) cells, none of them have fundamentally addressed the problem of limited emission budget.

Here we introduce MINFLUX, a concept for establishing the coordinates of a molecule with (minimal) emission fluxes, originating from a local excitation minimum. Compared to centroid-based localization, MINFLUX attains nanoscale precision with a much smaller number of detected photons N and records molecular trajectories with >100-fold higher temporal resolution (*24*). Moreover, our concept is surprisingly simple and can be realized in both scanning beam and standing wave microscopy arrangements.

Basic concept

In a background-free STED fluorescence microscope with true molecular (1 nm) resolution, detecting a single photon from the position of the doughnut zero is enough to identify a molecule at that coordinate (*25*). Detecting more than one photon is redundant. Consider a *gedanken* experiment in which we seek to establish the trajectory of a molecule diffusing in space. Instead of using uniform widefield excitation and a camera, we now excite with a reasonably bright focal doughnut that can be moved rapidly throughout the focal plane. If we now managed to target the zero of the doughnut-shaped excitation beam exactly at the molecule, steering it so that it is constantly overlapped with the molecule in space, the doughnut-targeting device would map the molecular trajectory without eliciting a single emission. On the other hand, a single emission (e.g., due to a minimal misplacement) would be enough to know that the molecule is not at the location of the doughnut zero.

Unfortunately, we cannot place the doughnut zero right at the molecular coordinate in a single shot, which is why perfect localization without emissions can be performed only by a supernatural being, a demon who knows the position of the molecule in advance. Yet, this *gedanken* experiment suggests that approaching the molecular position by targeting the zero of the excitation doughnut to the molecule should reduce the number of detected photons required for localization. This is because the position of the doughnut zero is well-defined and the resulting fluorescence indicates the residual distance of the molecule to the zero. Hence, apart from confirming the presence of the molecule, the resulting fluorescence carries information about the molecule's location. On the other hand, the fluorescence can be seen as the price to be paid for not matching the molecular position with that of the zero, which also implies that the smaller the mismatch is the fewer fluorescence photons are needed for localization.

Therefore, in a realization of MINFLUX (*26, 27*), the lo-

cation of the molecule is probed with a deep intensity minimum while the fluorescence emissions reveal the position of the molecule. Clearly, this strategy entails a favorable fluorescence photon economy: the approximate position is 'injected' by the excitation photons abundantly available from the light source (*25*), whereas the precious emitted photons are used just for fine-tuning.

MINFLUX can be implemented with many types of patterns, including standing waves which, after localizing in one dimension (1D), can be rotated to localize in other directions, too. Nonetheless, some key characteristics of MINFLUX hold for any pattern. To derive them, we now assume an arbitrary 1D intensity pattern $I(x)$ with $I(0) = 0$. This could be a standing wave (Fig. 1A) of wavelength λ, but we explicitly make no restrictions as to the pattern shape. Let us first probe the location x_m of a molecule, ignoring photon statistics. If the pattern is moved, such that the zero sweeps over the probing range $-L/2 < x < L/2$, the molecular fluorescence $f(x) = CI(x_m - x)$ vanishes at x_m. C is a prefactor that is proportional to the molecular brightness and the detection sensitivity, as well as to a parameter describing the molecular orientation in space. The solution x_m is now easily obtained by solving $f(x_m) = 0$.

Since C is a prefactor, the molecular orientation has no influence on the solution. This contrasts with camera-based localization, where unidentified molecular orientations can induce systematic errors in the tens of nanometer range (*12, 13*). Moreover, because $I(x)$ is known or can be determined experimentally, two probing measurements with the zeros of $I(x)$ placed around the molecule are sufficient for establishing x_m (Fig. 1B). Clearly, this also holds for the two 'endpoints' of the L-sized probing range, where the signal is given by $f_0 = CI(x_m + L/2) = CI_0(x_m)$ and $f_1 = CI(x_m - L/2) = CI_1(x_m)$; note that we have redefined the two displaced intensity functions with the subscripts 0 and 1. If L is so small that $f(x)$ can be approximated quadratically around x_m, any dependence on λ disappears. $f(x_m) = C(x_m - x^2) = 0$ then yields the solution $x_m = L\left[1/\left(1+\sqrt{f_1/f_0}\right) - 1/2\right]$ (see supplementary note 3). Thus, for small distances between the zero and the molecular position ($L << \lambda/\pi$), the solution x_m does not depend on the wavelength creating the light pattern. x_m does not depend on the fluorescence emission wavelength either, because the emitted photons are just collected. Therefore, in the quadratic approximation, the solution of the molecular position x_m does not depend on any wavelength.

In practice, f_0 and f_1 are the averages of the acquired photon counts n_0 and n_1 obeying Poissonian statistics, which needs to be considered. Hence, x_m is actually the expected value of the localization with the individual measurements fluctuating around this value. The conditional probability

distribution of photons $P(n_0,n_1|N)$ follows a binomial distribution $P(n_0,n_1|N) \approx \mathrm{Binomial}(p_0,N)$, where p_0 is the probability of assigning a photon to the first probing measurement I_0. This success probability is given by $p_0(x) = f_0(x)/[f_0(x) + f_1(x)] = I_0(x)/[I_0(x) + I_1(x)]$ considering the dependence on both $I(x)$ and L. We calculated $p_0(x)$ for three distances $L = 50, 100, 150$ nm of a standing wave of $\lambda = 640$ nm, showing that between $x = -L/2$ and $x = L/2$ it steeply spans the whole range between zero and unity (Fig. 1C). With decreasing L, the steepness increases and, in the quadratic approximation, we have $p_0(x) = \frac{1}{2}(2x/L+1)^2 / \left[(2x/L)^2 + 1 \right]$.

The position of the emitter x_m can be estimated using a maximum likelihood approach. The maximum likelihood estimator (MLE) of $\hat{x}_m$ is such that $p_0(\hat{x}_m) = n_0 / (n_0 + n_1) = \hat{p}_0$, where $\hat{p}_0$ is the MLE of the success probability $p_0(x_m)$. Thus $p_0(x)$ maps the statistics of n_0 and n_1 into the position estimation, giving the distribution of the position estimator $P(\hat{x}_m | N,L)$. The smaller L is, the more sharply distributed is $\hat{x}_m$ (Fig. 1C). Statistical modeling of MINFLUX allows us to calculate the Fisher information of the emitter position and its Cramér-Rao bound (CRB, see supplementary note 1), which determines the best localization precision attainable with any unbiased estimator (Fig. 1D). For the quadratic approximation, the CRB is given by $\sigma_{CRB}(x) = L/(4\sqrt{N})[(2x/L)^2 + 1]$ (eq. (S22b)). Unlike in camera-based localization, where the precision is homogeneous throughout the field of view, here it reaches a minimal value $\sigma_{CRB}(0) = L/(4\sqrt{N})$ (Fig. 1D) at the center of the probing range. Note that, for example, two measurements with the zero targeted to coordinates within a distance $L = 50$ nm localize a molecule with ≤ 2.5 nm precision using just 100 detected photons.

Analytical expressions of $p_0(x)$ and $\sigma_{CRB}(x)$ are equally well derived for doughnut beams and other types of patterns, as well as extended in 2D (fig. S1 and supplementary note 2). In fact, a doughnut excitation beam displays similar mathematical behavior around its minimum as a standing wave, but provides 2D information. Moreover, it can be combined with confocal detection for background suppression. Hence, we decided to explore the MINFLUX concept in a scanning confocal arrangement featuring a doughnut-shaped excitation beam, similarly to our *gedanken* experiment (Fig. 2A). Moving the doughnut across a large sample area ($\sim 20 \times 20$ μm^2) was realized by piezoelectric beam deflection, whereas fine positioning was performed electro-optically (see fig. S13 and Materials and Methods). The latter allowed us to set the doughnut zero within <5 μs with $<<1$ nm precision to arbitrary coordinates $\overline{r}_i$, concomitantly defining the distance L (Fig. 2B).

2D MINFLUX localization requires at least three coordinates $\overline{r}_1$, $\overline{r}_2$, and $\overline{r}_3$ of the doughnut zero, preferably arranged as an equilateral triangle (Fig. 2B). Considerations and simulations show that adding a fourth doughnut right at the triangle center $\overline{r}_0$ helps remove ambiguities in the position estimation (see fig. S2 and supplementary note 2). Thus, a set of four emitted photon counts n_0, n_1, n_2, and n_3 corresponding to the four positions of the doughnuts yields the molecular location (x_m,y_m) within an approximate range of diameter L, referred to as the field of view (Fig. 2B). As we can move and zoom the field of view quickly, our setup entails three basic modes of operation: (i) fluorescence nanoscopy (Fig. 2C); (ii) short range tracking of individual emitters that move within the field of view (Fig. 2D); and (iii) long range tracking and nanoscopy in microns sized areas, where the field of view is shifted in space in order to cover the large areas (Fig. 2E).

The success probability $\overline{p}(\overline{r})$, which maps the statistics of n_0, n_1, n_2, and n_3 into the position estimation, is now a multivariate function as is the CRB of the estimator (see fig. S3 and supplementary note 2). Like in the one-dimensional case, the CRB scales linearly with L at the origin and the dependence on λ vanishes with increasing validity of the quadratic approximation. We employed two types of position estimators in our experiments. The MLE is used for imaging because its precision was found to converge to the CRB for $N = \sum n_i \gtrsim 100$ photons. If $N < 100$, as is the case for quick position estimation in tracking, a modified least mean square estimator (mLMSE) is more suitable and can be implemented directly in the electronics hardware. Since the mLMSE is biased, the recorded trajectories are corrected afterwards using a numerically unbiased mLMSE (numLMSE) (see fig. S9 and supplementary note 3).

Localization precision, nanoscopy, and molecular tracking
To investigate the localization precision of MINFLUX, we repeatedly localized a single fluorescent emitter at different positions throughout the field of view. We used an ATTO 647N molecule in reducing and oxidizing system (ROXS) buffer (*18*) and divided the field of view into an array of 35×35 pixels separated by 3 nm in both directions. The excitation intensity and pixel dwell time were chosen such that each pixel contained $\lesssim 2$ counts on average. A stack of ~ 6000 arrays allowed us to perform an MLE- and numLMSE-based MINFLUX localization on each pixel using varying subsets of N photons. Repeating this procedure with different N-sized subsets and comparing each result with the pixel coordinate provided the localization precision at that pixel as a function of N (Fig. 3A and fig. S8). At the center of an $L = 100$ nm field of view, $N = 500$ photons were sufficient for obtaining 2 nm precision (Fig. 3, A to D). Note that localization precision and localization error can be considered

equivalent as the bias (accuracy) of the position estimations is negligible. Generally, the precision obtained with MINFLUX is higher than that achievable by a camera (Fig. 3, D to E). The measurements also confirm the inverse square-root dependence on N (Fig. 3E). Throughout the field of view, the precision obtained with MINFLUX agrees very well with the CRB (Fig. 3, B and D), indicating that photon information has indeed been used optimally.

To investigate the resolution obtainable with MINFLUX nanoscopy, we set out to discern fluorophores on immobilized labeled DNA origamis (28) featuring distances of 11 nm and 6 nm from each other (Fig. 4). After identifying an origami by widefield microscopy, we moved it as close as possible to the center of the field of view $(\overline{r}_0)$. As fluorophores we used Alexa Fluor 647 which, in conjunction with suitable chemical environment (29), $\lambda = 405$ nm illumination for on-switching, and $\lambda = 642$ nm excitation light, provided the on-off switching rates needed for keeping all but one molecule non-fluorescent. Imaging was performed by identifying the position of each emitting molecule as it emerged stochastically within the field of view. We used $L = 70$ nm and $L = 50$ nm for the 11 nm and the 6 nm origami, respectively. By applying a hidden Markov model (HMM, see Materials and Methods) to the fluorescence emission trace, we discriminated the recurrent single molecule emissions from multiple molecule events and from the background. Recording n_0, n_1, n_2, and n_3 for each burst and applying MINFLUX on those with $N = \sum n_i \geq 500$ and ≥ 1000 for the 11 nm and the 6 nm origami, respectively, allowed us to assemble a map of localizations yielding nanoscale resolution images (Fig. 4). The measurement time duration was 50 s and ~2 min for the 11 nm and the 6 nm origami, respectively. Although the individual molecules emerged very clearly, we further applied a k-means cluster analysis to classify the localization events into nano-domains representing fully discerned molecules at 11 nm and 6 nm distance. MINFLUX clearly resolves the molecules at 6 nm distance with 100% modulation (Fig. 4N) proving that true molecular scale resolution has been reached at room temperature.

We also made a rigorous comparison of MINFLUX nanoscopy with PALM/STORM. For the latter, we considered a noise-free ideal camera, so as to obtain optimal performance irrespective of camera characteristics such as dark and gain-dependent noise. To this end, we redistributed the photon counts of each emission event of our MINFLUX images, so that each one comprised $N = 500$ or 1000 counts for the 11 nm and 6 nm origami, respectively. For each nano-domain, the spread (covariance) of the localizations was calculated and displayed as a bivariate Gaussian distribution centered on each nano-domain (Fig. 4, G and L). For PALM/STORM we also considered $N = 500$ and 1000 photons per measured

localization point for the larger and smaller origami, respectively. We then calculated an ideal PALM/STORM image using the CRB of camera-based localization under the conditions that the camera has no read-out noise and the signal to background ratio (SBR$_c$) is 500. For the 11 nm origami, we obtained a localization precision of $\sigma = 5.4$ nm by PALM/STORM and an average σ of 2.1 nm for MINFLUX (see supplementary note 4). For the 6 nm origami, the corresponding values were $\sigma = 3.8$ nm for PALM/STORM and just $\sigma = 1.2$ nm for the average MINFLUX precision. While the CRB-based PALM/STORM images represent ideal recordings, the MINFLUX data may still contain influences by sample drift and other experimental imperfections, implying that further improvements are possible. The comparison actually shows that for the same low number of detected photons, MINFLUX nanoscopy clearly resolves the individual molecules, unlike PALM/STORM.

We note that a substantial fraction of Alexa Fluor 647 molecules can yield more than 500 or 1000 detected photons per emission cycle and, provided that these molecules are fortuitously used, the localization precision in PALM/STORM can be higher, at least in principle. In practice, however, attaining ~1–2 nm precision has been precluded by the fact that collecting high photon numbers is associated with extended recording times and hence with sample drift. Moreover, reconstructing superresolution images with molecules providing large photon numbers only, implies that poorer emitters are discarded, which compromises image faithfulness. In any case, the fact that MINFLUX requires much fewer detected photons should open the door for using switchable fluorophores providing fewer fluorescence photons.

Next we tracked single 30S ribosomal subunit proteins fused to the photoconvertible fluorescent protein mEos2 (30) in living *Escherichia coli* (Fig. 5A). MINFLUX tracking became possible after ensuring that (i) the switched-on molecules were in the field of view, (ii) the four-doughnut measurement was carried out so fast, that it was hardly blurred by motion, and (iii) the molecular position was estimated so quickly that repositioning the field of view kept the molecule largely centered. Additionally, the tracking algorithm had to be robust against losing the molecule by blinking (irregular mEos2 on and off intermittencies of 2.2 ms and 0.6 ms average duration, respectively—see fig. S12E and Materials and Methods). These hurdles were overcome by implementing position estimation and decision-making routines in hardware (Fig. 2A, see Material and Methods) which, together with our electro-optical and piezoelectric beam steering devices, provided a ~µs response time across a micrometer in an overall observation area of several tens of microns (Fig. 2E). The localization frequency of MINFLUX was set to 8 kHz and the mLMS and numLMS

position estimators were used in the live and post recording stages, respectively.

A collection of 1535 single molecule tracks was recorded from 27 living *E. coli* cells. Typical measured trajectories (Fig. 5, B to E) show that the central $(\overline{r}_0)$ doughnut produces a lower count rate, indicating that a single molecule is well centered while tracking. The reconstructed trajectories are naturally constituted of short ~ms traces (Fig. 5C), as the localization procedure is repeatedly interrupted by blinking of the fluorescent probe. The on and off states were identified by applying an HMM to the total collected photons per time interval (see Materials and Methods), thus discriminating the valid localizations.

For each trajectory, the apparent diffusion coefficient D and the localization precision σ were estimated for sliding windows of 35 ms. Both parameters were obtained from optimal least square fits (OLSF) of the mean square displacement (MSD, see supplementary note 5). The time dependence of D (Fig. 5D) reveals transient behavioral changes with unprecedented (so far 35 ms) temporal resolution for these kinds of fluorescent probes. It is worth noting that each point of this curve uses more than 100 valid localizations, which greatly surpasses the typical trajectory length ($\lesssim 15$ samples, see table S2) of classical camera tracking with single fluorescent proteins.

Plotting the mean localization precision σ against the mean number of photons per localization N (Fig. 5H) proves that the photon efficiency of MINFLUX tracking is 5- to 10-fold higher than that of its camera-based counterpart (even for an ideal detector, see fig. S6 and supplementary note 4). A mean localization precision of <48 nm was obtained by detecting, on average, just 9 photons per localization with a time resolution Δt of 125 µs. MINFLUX tracking was primarily limited by the blinking of mEos2, as it prevents the molecule from being tightly followed by the center of the beam pattern, where photon efficiency is the highest. A non-blinking probe would then be tracked more closely to the center, allowing for a smaller pattern size L and further reducing the average tracking error.

Any method that tracks a finite photon-budget probe will suffer from a tradeoff between the number of localizations in a track S and the spatial resolution σ. Our MINFLUX tracking experiments have been tuned in favor of high numbers of localizations, since it has been shown to be the best strategy for the measurement of D (*31*). This can be appreciated in the contour levels of the relative CRB of D, $\sigma_D^{\mathrm{CRB}} / D$ (Fig. 5I), as a function of the number of localizations S and the so-called reduced squared localization precision $X = \sigma^2/D\Delta t - 2R$ [R: blurring coefficient, (*32*)]. The latter can be thought of as the squared localization precision in units of the diffusion length within the integration time.

In this *X-S* plane, a scatter plot represents each measured trajectory (red), using average values per track. The average trajectory length was 157 ms with 742 valid localizations (which represents a ~100-fold improvement, see table S2), with a photon budget of ~5800 collected photons. Thereby, half of the obtained MINFLUX tracks show $\sigma_D^{\mathrm{CRB}} / D$ values below 23% ($S > 500$, Fig. 5I, inset). MINFLUX tracking can measure apparent diffusion coefficients with precisions <20%, while camera-based implementations (gray ellipse) center around 70%.

Discussion and outlook

Among the reasons why MINFLUX excels over centroid-based localization is that, in the latter, the origin of any detected photon has a spatial uncertainty given by the diffraction limit; in MINFLUX each detected photon is associated with an uncertainty given by the size L. Hence, adjusting L below the diffraction limit renders the emitted photons more informative. A perfect example is the origami imaging (Fig. 4) where adjusting L from 70 nm to 50 nm improves the localization precision substantially. However, making L smaller must not be confused with exploiting external a priori information about molecular positions; no Bayesian estimation approach is needed. MINFLUX typically starts at the diffraction limit, but as soon as some position information is gained, L can be reduced and the uncertainty range "zoomed in," making the detected photons continually more informative. Therefore, we can also regard MINFLUX as an acronym for maximally informative luminescence excitation probing. While we have not really exploited the zooming-in option here, decreasing L repeatedly during the localization procedure will further augment the power of MINFLUX, also eliminating the anisotropies prevalent at large L (Figs. 3C, 4G, and 5L). Iterative MINFLUX variants bear enormous potential for investigating macromolecules or interacting macromolecular complexes, potentially rivaling current Förster resonance energy transfer (*33*) and camera-localization-based approaches to structural biology (*34*).

Like in any other concept operating with intensity minima, the practical limits of MINFLUX will be set by background and aberrations blurring the intensity zero of $I(x)$. In our experiments, the doughnut minimum amounted to <0.2% of the doughnut crest (fig. S7). Regarding aberration corrections, in camera-based localization one has to correct a faint single molecule emission wavefront containing a few tens or hundreds photons of broad spectral range (100-200 nm), whereas in MINFLUX the corrections are applied to the bright and highly monochromatic (laser) wavefront producing $I(x)$, making the application of spatial light modulators straightforward. Moreover, the correction has to be optimized for the L-defined range only. This brings about the important advantage that in iterative MINFLUX imple-

mentations it is sufficient to compensate aberrations in the last (smallest L) iteration step, where their effect is minimal.

Spatial wavefront modulators can also be used to target the coordinates $\bar{r}_i$ with patterns $I_i(x)$ of varying shape and intensity, which is another degree of freedom for engineering the field of view toward uniform localization precision and for adapting the field of view toward the molecular motion. Since we have already achieved molecular scale resolution with the standard fluorophores, the new frontiers of MINFLUX will not be given by the resolution values but by the number of photons needed to attain that (single nanometer digit) resolution. Conversely, we can expect MINFLUX to enable tracking and nanoscopy of fluorophores that provide much fewer emissions, including auto- and other types of luminophores.

A fundamental difference between MINFLUX and STED nanoscopy is that in the latter, the doughnut pattern simultaneously performs both the localization and the on-off transition. Creating on-off state disparities between two neighboring points requires intensity differences that are large enough to create the off (or on) state with certainty. Since in MINFLUX nanoscopy the doughnut is used just for localization, such definite (i.e., saturated) transitions are not required.

Given that probing with an intensity maximum and solving for $\max[f = CI(x)]$ is equally possible, it is interesting to ask whether the same localization precision can be achieved in this case. The answer is no, because at a local emission maximum, small displacements of the emitter will not induce detection changes of similar significance for a small distance L (fig. S4). Yet, it will be possible to accommodate multiple fields of view in parallel using arrays of minima provided by many doughnuts or standing waves. Further expansions of our work include multicolor, 3D localization [e.g., by using a z-doughnut (2)], discerning emission spectra, polarization, or lifetime. Besides providing isotropic molecular resolution, such expansions should enable observation of inter- and intraprotein dynamics at their characteristic time scales. MINFLUX can also be implemented in setups featuring light sheet illumination (35), optical tweezers (36) and anti-Brownian electrokinetic trapping (37). In fact, MINFLUX should become the method of choice in virtually all experiments that localize single molecules and are limited by photon budgets or slow recording, such as the method called PAINT (22). Since it keeps or even relaxes the requirements for sample mounting, our concept should be widely applicable not only in the life sciences but also in other areas where superresolution and molecular tracking bear strong potential.

Finally, it is worthwhile reflecting on the fact that MINFLUX nanoscopy has attained the resolution scale ($\lesssim 6$ nm) where fluorescence molecules start to interact with each other—the ultimate limit attainable with fluorophores. While fluorescence on-off switching remains the cornerstone for breaking the diffraction barrier, in MINFLUX this breaking is augmented by the fact that, for small distances between a molecule and the intensity zero, the emitter localization does not depend on any wavelength. A consequence of this finding is that superresolution microscopy should also be expandable to low numerical aperture lenses, wavelengths outside the visible spectrum as well as to hitherto inapplicable luminophores. More staggering, however, is the implication that focusing by itself is becoming obsolete, meaning that it should be possible to design microscopy modalities with molecular (1 nm) resolution without employing a single lens.

References and Notes
1. S. W. Hell, J. Wichmann, Breaking the diffraction resolution limit by stimulated emission: Stimulated-emission-depletion fluorescence microscopy. *Opt. Lett.* **19**, 780–782 (1994). doi:10.1364/OL.19.000780 Medline
2. T. A. Klar, S. Jakobs, M. Dyba, A. Egner, S. W. Hell, Fluorescence microscopy with diffraction resolution barrier broken by stimulated emission. *Proc. Natl. Acad. Sci. U.S.A.* **97**, 8206–8210 (2000). doi:10.1073/pnas.97.15.8206 Medline
3. E. Betzig, G. H. Patterson, R. Sougrat, O. W. Lindwasser, S. Olenych, J. S. Bonifacino, M. W. Davidson, J. Lippincott-Schwartz, H. F. Hess, Imaging intracellular fluorescent proteins at nanometer resolution. *Science* **313**, 1642–1645 (2006). doi:10.1126/science.1127344 Medline
4. M. J. Rust, M. Bates, X. Zhuang, Sub-diffraction-limit imaging by stochastic optical reconstruction microscopy (STORM). *Nat. Methods* **3**, 793–796 (2006). doi:10.1038/nmeth929 Medline
5. S. T. Hess, T. P. K. Girirajan, M. D. Mason, Ultra-high resolution imaging by fluorescence photoactivation localization microscopy. *Biophys. J.* **91**, 4258–4272 (2006). doi:10.1529/biophysj.106.091116 Medline
6. S. W. Hell, Far-field optical nanoscopy. *Science* **316**, 1153–1158 (2007). doi:10.1126/science.1137395 Medline
7. H. Deschout, F. Cella Zanacchi, M. Mlodzianoski, A. Diaspro, J. Bewersdorf, S. T. Hess, K. Braeckmans, Precisely and accurately localizing single emitters in fluorescence microscopy. *Nat. Methods* **11**, 253–266 (2014). doi:10.1038/nmeth.2843 Medline
8. W. Heisenberg, *The Physical Principles of the Quantum Theory* (Chicago Univ. Press, Chicago, 1930).
9. N. Bobroff, Position measurement with a resolution and noise-limited instrument. *Rev. Sci. Instrum.* **57**, 1152–1157 (1986). doi:10.1063/1.1138619
10. R. E. Thompson, D. R. Larson, W. W. Webb, Precise nanometer localization analysis for individual fluorescent probes. *Biophys. J.* **82**, 2775–2783 (2002). doi:10.1016/S0006-3495(02)75618-X Medline
11. K. I. Mortensen, L. S. Churchman, J. A. Spudich, H. Flyvbjerg, Optimized localization analysis for single-molecule tracking and super-resolution microscopy. *Nat. Methods* **7**, 377–381 (2010). doi:10.1038/nmeth.1447 Medline
12. J. Engelhardt, J. Keller, P. Hoyer, M. Reuss, T. Staudt, S. W. Hell, Molecular orientation affects localization accuracy in superresolution far-field fluorescence microscopy. *Nano Lett.* **11**, 209–213 (2011). doi:10.1021/nl103472b Medline
13. M. D. Lew, M. P. Backlund, W. E. Moerner, Rotational mobility of single molecules affects localization accuracy in super-resolution fluorescence microscopy. *Nano Lett.* **13**, 3967–3972 (2013). doi:10.1021/nl304359p Medline
14. A. Yildiz, J. N. Forkey, S. A. McKinney, T. Ha, Y. E. Goldman, P. R. Selvin, Myosin V walks hand-over-hand: Single fluorophore imaging with 1.5-nm localization. *Science* **300**, 2061–2065 (2003). doi:10.1126/science.1084398 Medline
15. J. Elf, G.-W. Li, X. S. Xie, Probing transcription factor dynamics at the single-molecule level in a living cell. *Science* **316**, 1191–1194 (2007). doi:10.1126/science.1141967 Medline
16. A. Kusumi, T. A. Tsunoyama, K. M. Hirosawa, R. S. Kasai, T. K. Fujiwara, Tracking single molecules at work in living cells. *Nat. Chem. Biol.* **10**, 524–532 (2014).

doi:10.1038/nchembio.1558 Medline

17. S. J. Sahl, M. Leutenegger, M. Hilbert, S. W. Hell, C. Eggeling, Fast molecular tracking maps nanoscale dynamics of plasma membrane lipids. *Proc. Natl. Acad. Sci. U.S.A.* **107**, 6829–6834 (2010). doi:10.1073/pnas.0912894107 Medline

18. J. Vogelsang, R. Kasper, C. Steinhauer, B. Person, M. Heilemann, M. Sauer, P. Tinnefeld, A reducing and oxidizing system minimizes photobleaching and blinking of fluorescent dyes. *Angew. Chem. Int. Ed. Engl.* **47**, 5465–5469 (2008). doi:10.1002/anie.200801518 Medline

19. Q. Zheng, M. F. Juette, S. Jockusch, M. R. Wasserman, Z. Zhou, R. B. Altman, S. C. Blanchard, Ultra-stable organic fluorophores for single-molecule research. *Chem. Soc. Rev.* **43**, 1044–1056 (2014). doi:10.1039/C3CS60237K Medline

20. S. Weisenburger, B. Jing, D. Hänni, L. Reymond, B. Schuler, A. Renn, V. Sandoghdar, Cryogenic colocalization microscopy for nanometer-distance measurements. *ChemPhysChem* **15**, 763–770 (2014). doi:10.1002/cphc.201301080 Medline

21. A. Sharonov, R. M. Hochstrasser, Wide-field subdiffraction imaging by accumulated binding of diffusing probes. *Proc. Natl. Acad. Sci. U.S.A.* **103**, 18911–18916 (2006). doi:10.1073/pnas.0609643104 Medline

22. M. Dai, R. Jungmann, P. Yin, Optical imaging of individual biomolecules in densely packed clusters. *Nat. Nanotechnol.* **11**, 798–807 (2016). doi:10.1038/nnano.2016.95 Medline

23. J. V. Pellegrotti, G. P. Acuna, A. Puchkova, P. Holzmeister, A. Gietl, B. Lalkens, F. D. Stefani, P. Tinnefeld, Controlled reduction of photobleaching in DNA origami-gold nanoparticle hybrids. *Nano Lett.* **14**, 2831–2836 (2014). doi:10.1021/nl500841n Medline

24. A. Sanamrad, F. Persson, E. G. Lundius, D. Fange, A. H. Gynnå, J. Elf, Single-particle tracking reveals that free ribosomal subunits are not excluded from the *Escherichia coli* nucleoid. *Proc. Natl. Acad. Sci. U.S.A.* **111**, 11413–11418 (2014). doi:10.1073/pnas.1411558111 Medline

25. S. W. Hell, Nanoscopy with focused light (Nobel Lecture). *Angew. Chem. Int. Ed. Engl.* **54**, 8054–8066 (2015). doi:10.1002/anie.201504181 Medline

26. S. W. Hell, Method of and apparatus for tracking a particle, particularly a single molecule, in a sample. Patent application WO 2013/072273 A1 B2, 23 May 2013.

27. S. W. Hell, High-resolution fluorescence microscopy with a structured excitation beam. Patent application WO 2015/097000 A1, 2 July 2015.

28. J. J. Schmied, A. Gietl, P. Holzmeister, C. Forthmann, C. Steinhauer, T. Dammeyer, P. Tinnefeld, Fluorescence and super-resolution standards based on DNA origami. *Nat. Methods* **9**, 1133–1134 (2012). doi:10.1038/nmeth.2254 Medline

29. G. T. Dempsey, J. C. Vaughan, K. H. Chen, M. Bates, X. Zhuang, Evaluation of fluorophores for optimal performance in localization-based super-resolution imaging. *Nat. Methods* **8**, 1027–1036 (2011). doi:10.1038/nmeth.1768 Medline

30. S. A. McKinney, C. S. Murphy, K. L. Hazelwood, M. W. Davidson, L. L. Looger, A bright and photostable photoconvertible fluorescent protein. *Nat. Methods* **6**, 131–133 (2009). doi:10.1038/nmeth.1296 Medline

31. C. L. Vestergaard, Optimizing experimental parameters for tracking of diffusing particles. *Phys. Rev. E Stat. Nonlin. Soft Matter Phys.* **94**, 022401 (2016). doi:10.1103/PhysRevE.94.022401 Medline

32. X. Michalet, A. J. Berglund, Optimal diffusion coefficient estimation in single-particle tracking. *Phys. Rev. E Stat. Nonlin. Soft Matter Phys.* **85**, 061916 (2012). doi:10.1103/PhysRevE.85.061916 Medline

33. B. Schuler, E. A. Lipman, W. A. Eaton, Probing the free-energy surface for protein folding with single-molecule fluorescence spectroscopy. *Nature* **419**, 743–747 (2002). doi:10.1038/nature01060 Medline

34. A. Pertsinidis, Y. Zhang, S. Chu, Subnanometre single-molecule localization, registration and distance measurements. *Nature* **466**, 647–651 (2010). doi:10.1038/nature09163 Medline

35. A. H. Voie, D. H. Burns, F. A. Spelman, Orthogonal-plane fluorescence optical sectioning: Three-dimensional imaging of macroscopic biological specimens. *J. Microsc.* **170**, 229–236 (1993). doi:10.1111/j.1365-2818.1993.tb03346.x Medline

36. A. Ashkin, J. M. Dziedzic, J. E. Bjorkholm, S. Chu, Observation of a single-beam gradient force optical trap for dielectric particles. *Opt. Lett.* **11**, 288–290 (1986). doi:10.1364/OL.11.000288 Medline

37. A. E. Cohen, W. E. Moerner, Method for trapping and manipulating nanoscale objects in solution. *Appl. Phys. B* **86**, 093109 (2005).doi:10.1063/1.1872220

38. S. M. Kay, *Fundamentals of Statistical Signal Processing: Estimation Theory* (Prentice Hall, New Jersey, 1993), vol. 1.

39. F. Pukelsheim, *Optimal Design of Experiments* (SIAM, 1993), vol. 50.

40. J. E. Mosimann, On the compound multinomial distribution, the multivariate beta-distribution, and correlations among proportions. *Biometrika* **49**, 65–82 (1962).

41. F. Huang, T. M. P. Hartwich, F. E. Rivera-Molina, Y. Lin, W. C. Duim, J. J. Long, P. D. Uchil, J. R. Myers, M. A. Baird, W. Mothes, M. W. Davidson, D. Toomre, J. Bewersdorf, Video-rate nanoscopy using sCMOS camera-specific single-molecule localization algorithms. *Nat. Methods* **10**, 653–658 (2013). doi:10.1038/nmeth.2488 Medline

42. A. J. Berglund, Statistics of camera-based single-particle tracking. *Phys. Rev. E Stat. Nonlin. Soft Matter Phys.* **82**, 011917 (2010). doi:10.1103/PhysRevE.82.011917 Medline

43. B. Shuang, C. P. Byers, L. Kisley, L.-Y. Wang, J. Zhao, H. Morimura, S. Link, C. F. Landes, Improved analysis for determining diffusion coefficients from short, single-molecule trajectories with photoblinking. *Langmuir* **29**, 228–234 (2013). doi:10.1021/la304063j Medline

44. C. L. Vestergaard, P. C. Blainey, H. Flyvbjerg, Optimal estimation of diffusion coefficients from single-particle trajectories. *Phys. Rev. E Stat. Nonlin. Soft Matter Phys.* **89**, 022726 (2014). doi:10.1103/PhysRevE.89.022726 Medline

45. X. Michalet, Mean square displacement analysis of single-particle trajectories with localization error: Brownian motion in an isotropic medium. *Phys. Rev. E Stat. Nonlin. Soft Matter Phys.* **82**, 041914 (2010). Medline

46. M. Stracy, C. Lesterlin, F. Garza de Leon, S. Uphoff, P. Zawadzki, A. N. Kapanidis, Live-cell superresolution microscopy reveals the organization of RNA polymerase in the bacterial nucleoid. *Proc. Natl. Acad. Sci. U.S.A.* **112**, E4390–E4399 (2015). doi:10.1073/pnas.1507592112 Medline

47. W. Li, E. Bouveret, Y. Zhang, K. Liu, J. D. Wang, J. C. Weisshaar, Effects of amino acid starvation on RelA diffusive behavior in live *Escherichia coli*. *Mol. Microbiol.* **99**, 571–585 (2016). doi:10.1111/mmi.13252 Medline

48. S. Bakshi, A. Siryaporn, M. Goulian, J. C. Weisshaar, Superresolution imaging of ribosomes and RNA polymerase in live *Escherichia coli* cells. *Mol. Microbiol.* **85**, 21–38 (2012). doi:10.1111/j.1365-2958.2012.08081.x Medline

49. S. Manley, J. M. Gillette, G. H. Patterson, H. Shroff, H. F. Hess, E. Betzig, J. Lippincott-Schwartz, High-density mapping of single-molecule trajectories with photoactivated localization microscopy. *Nat. Methods* **5**, 155–157 (2008). doi:10.1038/nmeth.1176 Medline

Acknowledgments

Supplementary Materials

www.sciencemag.org/cgi/content/full/science.aak9913/DC1
Materials and Methods
Supplementary Text
Figs. S1 to S14
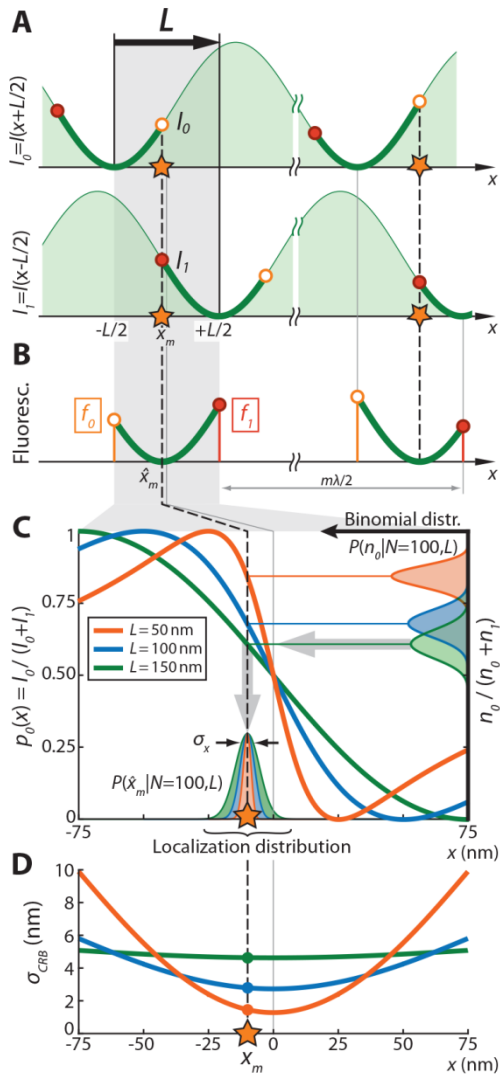Tables S1 and S2
References (*38–49*)

Fig. 1. Principles of MINFLUX illustrated in a single dimension (x) using a standing light wave of wavelength λ. (A) The unknown position x_m of a fluorescent molecule is determined by translating the standing wave, such that one of its intensity zeros travels from $x = -L/2$ to $L/2$ to, with x_m being somewhere in between. (B) Since the molecular fluorescence $f(x)$ becomes zero at x_m, solving $f(x_m) = 0$ yields the molecular position x_m. Equivalently, the emitter can also be located by exposing the molecules just to two intensity values belonging to functions $I_0(x)$ and $I_1(x)$ that are fixed in space having zeros at $x = -L/2$ and $L/2$, respectively. Establishing the emitter position can be performed in parallel with another zero, targeting molecules further away than $\lambda/2$ from the first one. (C) Localization considering the statistics of fluorescence photon detection: success probability $p_0(x)$ for beam separations L of 50 nm of (orange), 100 nm (blue) and 150 nm (green) for $\lambda = 640$ nm. The fluorescence photon detection distribution $P(n_0|N = n_0 + n_1 = 100)$ conditioned to a total of 100 photons is plotted along the right vertical axis of normalized detections $n_0|N$ for each L. The distribution of detections is mapped into the position axis x through the corresponding $p_0(x,L)$ function (gray arrows), delivering the localization distribution $P(\hat{x}_m \mid N = 100)$.

The position estimator distribution contracts as the distance L is reduced. (D) Cramér Rao bound for each L. Precision is maximal halfway between the two points where the zeros are placed. For $L = 50$ nm, detecting just 100 photons yields a precision of 1.3 nm.
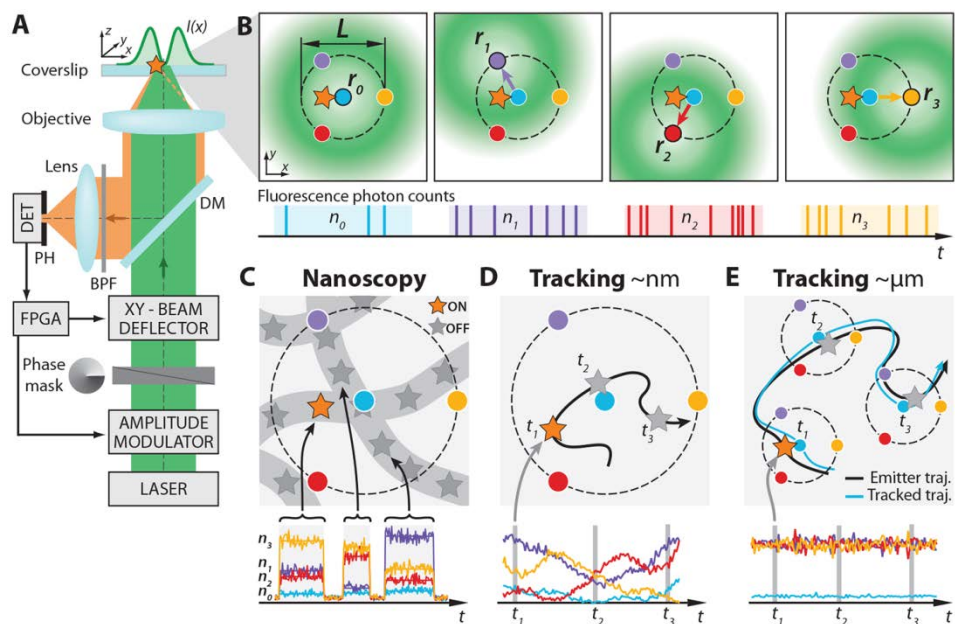
Fig. 2. Setup, measurement strategy, and various application fields of the two-dimensional MINFLUX implementation. (**A** and **B**) Simplified setup (details in Materials and Methods). An excitation laser beam (green) is shaped by a vortex phase mask forming a doughnut intensity spot in the focal plane of the objective lens. The intensity of the beam is modulated and deflected such that its central zero is sequentially placed at the four focal plane positions $\overline{r}_{0,1,2,3}$, indicated by blue, violet, red, and yellow dots, respectively. Photons emitted by the fluorescent molecule (star) are collected by the objective lens and directed toward a fluorescence bandpass filter (BPF) and a confocal pinhole (PH), using a dichroic mirror (DM). The fluorescence photons $n_{0,1,2,3}$ counted for each doughnut position $\overline{r}_{0,1,2,3}$ by the detector (DET) are used to extract the molecular location. Intensity modulation and deflection, as well as the photon counting are controlled by a field-programmable gate array (FPGA). (**C** to **E**) Basic application modalities of MINFLUX. (C) Nanoscopy: a nanoscale object features molecules whose fluorescence can be switched on and off, such that only one of the molecules is on within the detection range. They are distinguished by abrupt changes in the ratios between the different $n_{0,1,2,3}$ or by intermissions in emission. (D) Short (nanometer) range tracking: the same procedure can be applied to a single emitter that moves within the localization region of size L. As the emitter moves, different ratios are observed that allow the localization. (E) Long (microns) range tracking: if the emitter leaves the initial L-sized field of view, the triangular set of positions of the doughnut zeros is (iteratively) displaced to the last estimated position of the molecule. By keeping it around $\overline{r}_0$ by means of a feedback loop, photon emission is expected to be minimal for n_0 and balanced between n_1, n_2, and n_3, as shown.
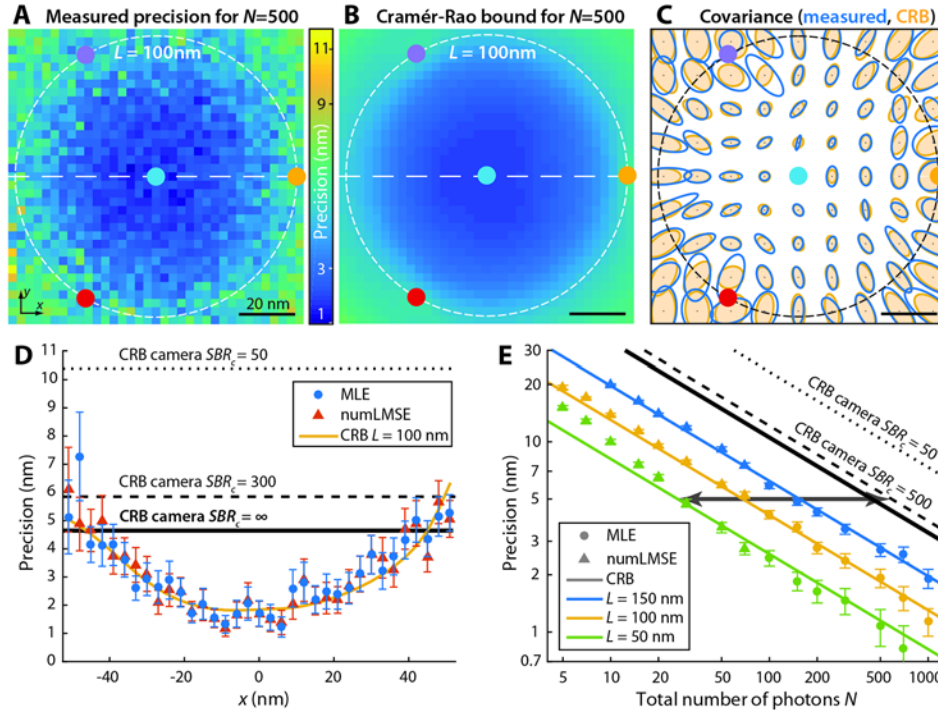
Fig. 3. Localization precision of MINFLUX measured on a single ATTO 647N molecule. (**A**) Measured localization precision obtained by maximum-likelihood estimation (MLE) based MINFLUX. The localization error reaches down to 2 nm for $n = 500$ detected photons using a beam separation of $L = 100$ nm. The signal-to-background ratio (SBR) was 13.6 at the central pixel. (**B**) The best precision possible (Cramér-Rao bound, CRB) under the same conditions as in (A). (**C**) Representation of the measured and theoretical localization uncertainty covariances (as ellipses of contour level $e^{-1/2}$), same conditions as in (A and B). (**D**) Measured localization precision along the x-axis in (A and B) for MINFLUX localization performed with the MLE (circles) and with the numerically unbiased position estimator (numLMSE, triangles), and the corresponding CRB of MINFLUX (yellow line). The CRB on the localization precision of an ideal camera with realistic signal-to-background ratio (dashed lines) is worse than that provided by MINFLUX (see supplementary note 4). The ultimate limit for the ideal camera (infinite SBR_c) is shown by the solid black line. (**E**) Localization precision at the center of the excitation pattern as a function of total number of detected photons N: decreasing the beam separation L improves the localization precision more effectively than increasing the number of detected photons; note the logarithmic scales. For the low photon regime ($N < 100$) the numerically unbiased position estimator (numLMSE, see supporting note 3.2.3) was employed, while the MLE was used for $N \geq 100$ detected photons. For most regimes, the measured MINFLUX localization precision reaches the theoretical limit under the measurement conditions (CRB, solid lines). For comparison, the CRB of an ideal camera localization is shown (dashed lines). The camera case of infinite SBR_c is shown by the solid black line. Measurement and theory show that obtaining a localization precision of 5 nm requires ~600 photon counts with an ideal camera ($SBR_c = 500$), while MINFLUX with $L = 50$ nm requires only ~27 photon counts [gray arrow in (E)].
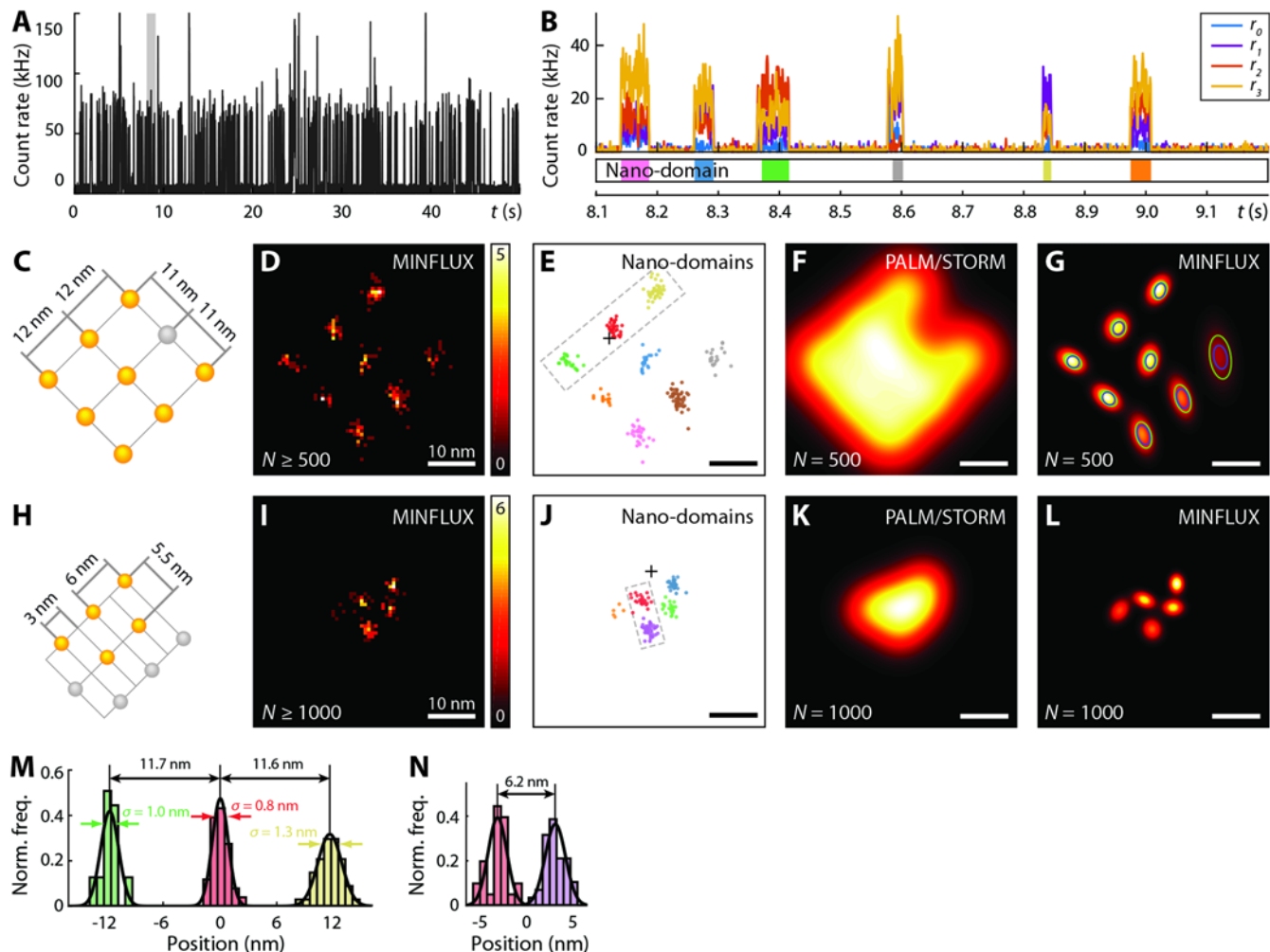
Fig. 4. MINFLUX nanoscopy of labeled DNA origamis. (**A**) Time trace of total photon count rate from a single DNA origami. Time bins: 1 ms. (**B**) Zoomed-in trace interval showing count rates for the four doughnut positions and the resulting classification of each localization in nano-domains (lower panel); color corresponds to the cluster assignments shown in (E). Time bins: 1 ms. (**C**) Arrangement of up to nine on-off switchable fluorophores on the origami (those remaining off throughout the measurement shown in gray). (**D**) Nanoscopy image rendered by spatial binning of direct MINFLUX localizations. Events yielding $N < 500$ detected photons were discarded. Bin size: 0.75 nm. (**E**) Scatter plot of MINFLUX localizations. The coloring shows the classification into nano-domains as described in (B). The dashed gray line indicates the region for the profile displayed in (M). The position of the central doughnut zero $\overline{r_0}$ is marked by a black cross. (**F** and **G**) Comparison between practical MINFLUX nanoscopy and ideal PALM/STORM imaging (simulated, see supporting note 4) of the origami using $N = 500$ photons. The rendering shows bivariate normal distributions with the experimental or theoretical covariance, respectively. The green and blue ellipses in (G) illustrate the $e^{-1/2}$ level (diameter $=2\sigma$) of the experimental covariance and the Cramér-Rao bound (CRB), respectively. (**H** to **L**) Analogous to (C to G) for the smaller DNA origami sketched in (H). Events yielding $N < 1000$ detected photons were discarded. (**M**) Projected line profile of the larger origami (C) as indicated by the dashed gray rectangle in (E). Bin size: 0.75 nm. (**N**) Projected line profile of the smaller DNA origami as indicated by the dashed gray rectangle in (J). Bin size: 0.75 nm. Owing to its higher localization precision, MINFLUX nanoscopy displays fundamentally improved resolution over PALM/STORM, reaching single nanometer resolution with $N = 500$ photons at room temperature.
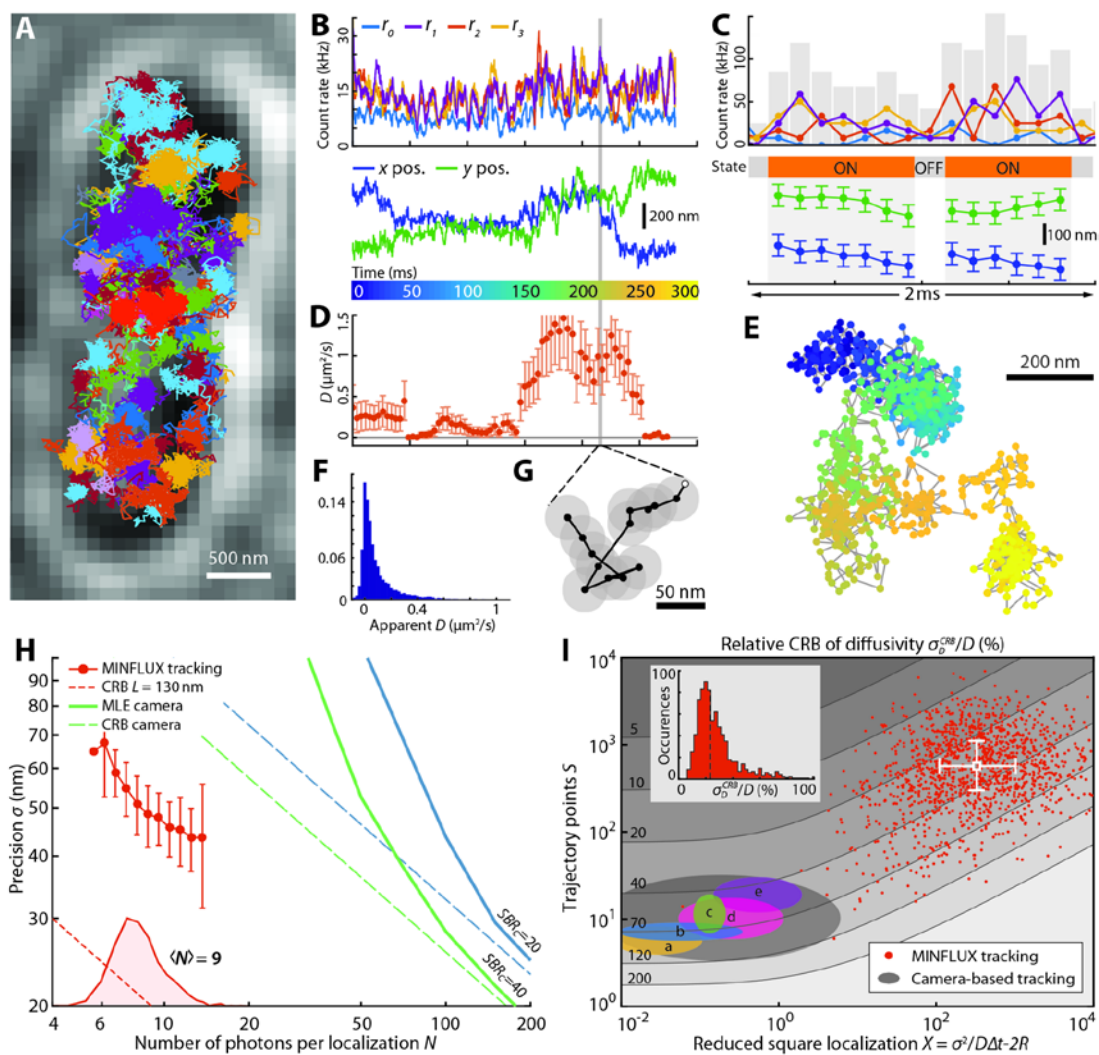
Fig. 5. Single-molecule MINFLUX tracking in living *E. coli* bacteria. Single 30*S* ribosomal protein subunits fused to the switchable fluorescent protein mEos2 are tracked. (**A**) Transmission image of a bacterium overlaid with 77 independent tracks. (**B**) Details of a track. Upper panel: low pass filtered count rate of the four exposures (blue: $\overline{r}_0$, violet: $\overline{r}_1$, red: $\overline{r}_2$, yellow: $\overline{r}_3$), average total count rate 52 kHz. *Lower panel*: extracted *x* and *y* coordinates of the trajectory. (**C**) 2 ms excerpt of the trace in (B) (marked in gray at time point 210 ms). *Upper panel*: counts per exposure are shown together with their sum (gray bars) used for on/off classification. *Middle panel*: on/off classification. *Lower panel*: Extracted *x* and *y* coordinates [cf. (G)]; the average tracking error is 48 nm. (**D**) Apparent diffusion constants *D* for a sliding window of 35 ms with their approximated error bars. (**E** and **G**) Trajectories shown in (B) and (C), respectively. The diameter of the shaded circles in (G) visualize the average tracking error. (**F**) Normalized occurrences of apparent diffusion constants *D* for all measured tracks. (**H**) Mean localization precision σ vs. average counts per MINFLUX localization *N* for all measured tracks (red circles, marginal distribution of *N* plotted along the horizontal axis), CRB of MINFLUX static localization for the measuring condition *L* = 130 nm (red dashed), idealized static camera localization performance (CRB: dashed, MLE: line) for two relevant signal to background ratios SBR$_c$ of 20 and 40. (**I**) Contour lines of the relative CRB of the diffusivity $\sigma_D^{\mathrm{CRB}} / D$, as a function of the trajectory length *S* and the reduced localization precision *X*. The white cross shows the quartiles (25%, 50%, and 75%) of the marginal distributions of *S* and *X* for the experimental data. Simulations showed that the diffusion estimator, though not optimal, provides acceptable results (see fig. S10D and supplementary note 5). The gray ellipse represents how well the diffusion coefficient has been identified with state-of-the-art camera tracking of fluorescent proteins (colored ellipses refer to table S2). The inset shows the distribution of $\sigma_D^{\mathrm{CRB}} / D$ for tracks with more than 500 localizations (*S* > 500 encompasses ~50% of the data—see fig. S12C) and its median (dashed line, at 23%).

Nanometer resolution imaging and tracking of fluorescent molecules with minimal photon fluxes

Francisco Balzarotti, Yvan Eilers, Klaus C. Gwosch, Arvid H. Gynnå,
Volker Westphal, Fernando D. Stefani, Johan Elf and Stefan W. Hell
(December 22, 2016)
published online December 22, 2016

Editor's Summary

Article Tools	Visit the online version of this article to access the personalization and article tools: http://science.sciencemag.org/content/early/2016/12/21/science.aak9913
Permissions	Obtain information about reproducing this article: http://www.sciencemag.org/about/permissions.dtl